Two-phase gas-liquid flow in concentric and fully eccentric annuli.

Part I: Flow patterns, holdup, slip ratio and pressure gradient

Roberto Ibarra[a,*], Jan Nossen[b], Murat Tutkun[c]

Institute for Energy Technology (IFE), Kjeller, Norway, 2007

[a] *roberto.jose.ibarra-hernandez@ife.no*

[b] *jan.nossen@ife.no*

[c] *murat.tutkun@ife.no*

Corresponding author

Address: Department of Fluid Flow and Environmental Technology, Institute for Energy Technology, Instituttveien 18, Kjeller, Norway, 2007.

Telephone: +47 63 80 60 00

Abstract

Horizontal and upward low-inclination gas-water and gas-oil flows are investigated using an annulus pipe configuration in a high-pressure system (~400 kPa). The annulus test section, or the so-called pipe-in-pipe configuration, consists of an outer pipe of 99 mm inside diameter and an inner pipe of 50 mm outside diameter. Two different vertical positions of the inner pipe with respect to outer pipe have been tested; namely concentric configuration where both pipes have the same centreline and fully eccentric where the inner pipe is placed at the bottom wall of outer pipe. The flow is studied using high-speed photography, differential pressure transducers, and broad-beam gamma densitometers to characterise the flow as function of the liquid phase properties, annulus eccentricity, and pipe inclination. Flow regime maps reveal that slug flow appears to be the most common flow feature across the conditions studied in this paper. Flow in the eccentric annulus shows a more consistent behaviour (*i.e.* well-defined flow structures axially and in time) than that observed in the concentric annulus. Gas-oil flows show more stable phase fraction behaviour across the cross-section compared to that observed in gas-water flows in which the interface shows significant activity promoting the formation of droplets and ligaments that break from the liquid film. This is especially the case with the concentric annulus configuration. The oil phase regardless of the geometrical configuration tends to fully wet the pipe (made of PVC) as the gas velocity increases, creating a continuous film along the pipe walls. Conversely, the thin film in gas-water flow is not continuous. Discontinuity in the thin film increases with an increase in effective pipe roughness. Given the same inlet flow conditions, the concentric annulus configuration causes larger pressure drop along the pipe than that obtained in the eccentric.

1   Introduction

In April 2010, eleven people were killed on the Deepwater Horizon drilling platform in the Gulf of Mexico after an explosion. The rig sank and left the drilling riser on the sea floor leaking oil and gas from the reservoir through the gap between the riser (outer tube) and drillstring. Soon questions were raised about the volume of oil being released to the sea, and this number has played a large role in the court proceedings after the disaster. One of the techniques that were used to estimate the amount of oil spill was essentially running a dynamic multiphase flow simulator to match the recorded frequency of oil slugs (or plugs) releasing from the sunken riser.

Detailed examination of the simulator output has indicated that there are serious flaws in this approach. The most obvious one is the lack of accurate models for multiphase flow in an annulus, that is, the multiphase flow between the inner and the outer pipes. Commercial dynamic multiphase flow simulators lack the physics-based models which are necessary to predict pressure drop in annulus flow accurately, even for single-phase flow. In practice, well design is therefore based on oversimplifications (*e.g.* using the hydraulic diameter of the annulus in models developed for full pipe systems) leading to large uncertainties, causing higher risks in operation and prone to large errors in predictions.

Annulus flow occurs in oil wells when fluids like oil, gas, water and drilling fluids flow between the inner and outer pipes. Examples are flow between the production tubing and the outer casing, between a gas injector and the production tubing, or between coiled tubing (inserted into the well from above) and the production tubing.

Even though flow in annulus is relatively common in oil drilling, oil production and well interventions, our understanding of multiphase flow in annulus is very limited compared to what we know about multiphase flow in conventional circular pipes. To our knowledge there has been no experimental data or theoretical models published to describe multiphase annulus flow for large outer pipe diameters in high-pressure systems yet. Current knowledge in multiphase flow in annuli geometry is mainly based on experimental research on two-phase flow of low pressure air

and low viscosity liquids like kerosene and water, principally for vertical flow configurations (Kelessidis and Dukler, 1989; Caetano *et al.*, 1992a, b; Hasan and Kabir, 1992; Das *et al.*, 1999; Hibiki *et al.*, 2003; Ozar *et al.*, 2008; Julia *et al.*, 2011) as presented in Table 1. The gas-liquid flow in a horizontal annulus is limited to only a few research papers (Osamasali and Chang, 1988; Ekberg *et al.*, 1999; Wongwises and Pipathattakul, 2006; Ozbayoglu and Yuksel, 2012).

Table 1: Summary of studies in multiphase flow in annuli (see Section 2 for definition of the variables).

Study	D_1 (mm)	D_2 (mm)	E	θ (°)	Fluids	Measurement
Osamasali and Chang (1988)	51	19.1 to 31.9	0	0	Air-water	Flow regime map
Kelessidis and Dukler (1989)	76.2	50.8	0; 0.5	90	Air-water	Flow regime map
Caetano *et al.* (1992a)	76.2	42.2	0; 1	90	Air-water Air-kerosene	Flow regime map, friction factor, Taylor bubble velocity
Hasan and Kabir (1992)	127	48; 57; 87	0	58; 66; 74; 82; 90	Air-water	Void fraction, bubble rise velocity
Das *et al.* (1999)	25.4 38.1 50.8	12.7 12.7 25.4	0	90	Air-water	Flow regime map, phase distribution
Ekberg *et al.* (1999)	8.6 35.2	6.6 33.2	0	0	Air-water	Flow regime map, void fraction, pressure drop
Hibiki *et al.* (2003)	38.1	19.1	0	90	Air-water	Void fraction, interfacial velocity and area concentration, liquid velocity and turbulent intensity
Wongwises and Pipathattakul (2006)	12.5	8	0	0; 30; 60	Air-water	Flow regime map, void fraction, pressure drop
Ozar *et al.* (2008)	38.1	19.1	0	90	Air-water	Flow regime map, void fraction, interfacial velocity and area concentration
Julia *et al.* (2011)	38.1	19.1	0	90	Air-water	Flow regime map
Ozbayoglu and Yuksel (2012)	73.9	47	1	0	Air-water	Flow regime map, liquid holdup

Multiphase annulus flow is more complex than the one in circular pipe. The flow in annulus is subtly different from circular pipe flow, even for single-phase flow. For example, a concentric annulus yields a larger friction factor than a circular pipe with equivalent hydraulic diameter at similar Reynolds numbers. The opposite appears to be the case when an eccentric annulus is considered (Caetano *et al.*, 1992a, b). The critical Reynolds number for transition from laminar to turbulent flow depends not only on the surface properties of the pipe walls but also on the eccentricity. Flow in eccentric annulus is turbulent in the wider part of the gap and laminar in the narrower parts (Hanks and Bonner, 1971; Dou *et al.*, 2010). This complicates the calculation of pressure drop. Similar, or potentially stronger, effects of eccentricity are expected in multiphase flow in annuli, for example, Kelessidis and Dukler (1990) showed that the Taylor bubble in a vertical annulus is strongly asymmetric.

Acquiring accurate and detailed measurement data in multiphase flow, in particular cross-sectional data, is always complicated and proven to be rather difficult. This, however, is required for development of detailed mechanistic models. High-speed video cameras and conductivity probes have been the main instruments for measuring phase distribution in annulus so far (Ozar *et al.*, 2008; Ozbayoglu and Yuksel, 2012). It is, however, a big challenge to capture dynamic flow phenomena in an eccentric annulus geometry due to the narrow gap, asymmetry and overall complexity. The recent development in X-ray tomography and PIV systems (Hu *et al.*, 2009; Hu *et al.*, 2010; Sveen, 2013) have been very useful for capturing cross-sectional phase and velocity data.

Lack of high quality, industry-relevant multiphase flow data has led researchers to oversimplify the problem on hand, or to introduce too much dependency on empirical relations. In this situation, commercial simulators will inevitably be limited to the range of conditions at which correlations were developed. Extensive experimental data, partly presented herein, will certainly contribute to our understanding of annulus flow and let us develop more accurate and physical flow models.

The current paper is structured as follows. Section 2 describes the experimental setup, the flow conditions and procedure. The overall results in terms of flow regimes, liquid holdup and pressure gradient are presented and discussed in section 3. Finally, section 4 contains the conclusions of this work.

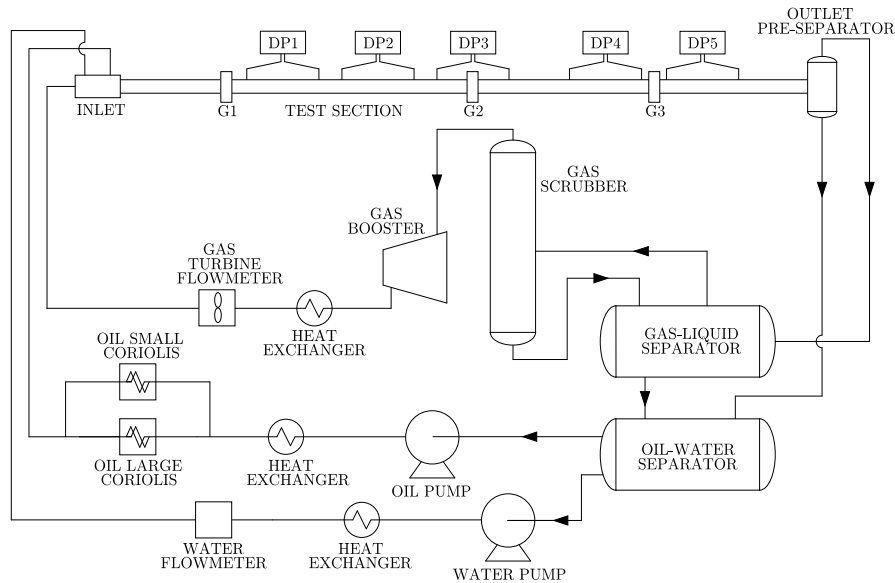## 2   Experimental Setup

2.1   *Annulus geometry*

Annulus flow is characterised by two parallel pipes where fluids flow through the cross-section between the inside wall of the outer pipe and the outside wall of the inner pipe as shown in Figure 1. The diameter ratio, $K = D_2/D_1$, and the relative position of the inner and outer pipe centres (*i.e.* degree of eccentricity, E) define the geometry, where D_1 is the inside diameter of the outer pipe and D_2 the outside diameter of the inner pipe. The degree of eccentricity is defined as $E = 2\delta/(D_1{-}D_2)$, where δ is the distance between pipe centres. Accordingly, the hydraulic diameter is defined as the difference between diameters, $D_h = D_1{-}D_2$ (*i.e.* based on the flow area and the wetted perimeter).
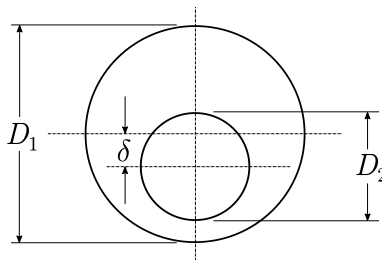
Figure 1: Annulus geometrical parameters.

2.2   *Flow facility*

The experimental investigations were performed in the Well Flow Loop (WFL) of IFE. Figure 2 shows the schematics of the Well Flow Loop, which can be used for both two-phase (gas-liquid or liquid-liquid) or three-phase flows.
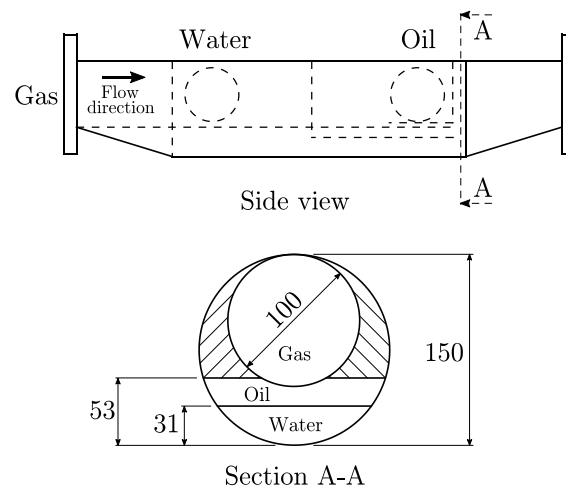
Figure 2: Schematic of the experimental flow loop (DP: differential pressure transducers, G1-3: gamma densitometers).

The flow loop consists of gas-liquid and liquid-liquid gravity-driven separators with a capacity of 0.8 m³ and 4 m³, respectively. The gas phase, from the gas-liquid separator, flows through a scrubber before entering the gas booster. The scrubber is operated to remove any liquid remaining in the gas stream. The gas booster (Spencer, Model GS24103C) consists of a three-stage impeller, driven by an electrical motor, with a capacity of 1000 Sm³/h. The gas volumetric flow rate is measured with a turbine flowmeter (Elster Quantometer Q1000) with an accuracy of ±1.5% of the reading. Two centrifugal pumps (ABS, Type ZLKC), with a capacity of 45 m³/h each, are used for the water and oil phases. The water volumetric flow rate is measured with an electromagnetic flowmeter (Fischer & Porter, Type 10 DX 3311A) with a capacity of 0 – 60 m³/h, and an accuracy of ±0.5% of the reading. The oil line is equipped with a set of two Coriolis mass flow meters (Danfoss, Type MASSFLO 10000) with capacities of 40 – 20000 and 80 – 40000 kg/h (0.05 – 25 and 0.1 – 50 m³/h based on the Exxsol D60 density) and accuracy of ±0.2% of the reading. The gas and liquid injection lines are equipped with heat exchangers to maintain the temperature of the fluids between ±1° during the experimental campaign.

The inlet of the test section consists of three chambers with splitter plates to promote stratification at the exit of the plates as shown in Figure 3. The gas phase is injected in-line with

the test section and flows through the upper chamber. The oil and water phases are injected from the side and flow through the centre and bottom chambers, respectively. A flow straightener is installed downstream of the inlet section to remove swirl generated by the inlet geometry configuration. The annulus test section, with a total length of 45 m, has an inside diameter of the outer pipe, D_1, of 99 mm and an outside diameter of the inner pipe, D_2, of 50 mm, resulting in a diameter ratio of $K = 0.505$. The material for both the outer and inner pipe is PVC with an absolute roughness of approximately 2 μm. Experiments cover concentric ($E = 0$) and fully eccentric ($E = 1$) annulus configurations with the inner pipe located at the bottom of the outer pipe. The inner pipe extends over the entire length of the test section and was positioned using specially designed (3D printed) wing shaped supports to minimise the effect on the flow. A post-fabrication surface treatment was performed to obtain a similar roughness that that of the inner and outer pipe (*i.e.* PVC).

Figure 3: Schematic of the inlet section (dimensions are in millimetres).

2.3   Flow conditions and experimental procedure

The test fluids were tap water and oil (Exxsol D60), as the liquid phases, and sulphur hexafluoride (SF$_6$), as the gas phase (Table 2 shows the physical properties of the test fluids). The SF$_6$ gas was selected due to its high density which is approximately 6 times higher than the density of air, allowing a better representation of the conditions found in, for example, offshore

gas-oil systems.

Table 2: Physical properties of the test fluids at ~400 kPa (abs.) and ~20 °C.

	Density, ρ (kg/m^3)	Viscosity, μ (mPa.s) at Atm	Surface tension, σ, to gas phase (mN/m)
SF$_6$ (gas)	23.9	0.015 ± 0.002	–
Exxsol D60	802	1.4 ± 0.02	28.8 ± 0.1
Tap water	998	1.04 ± 0.02	71.8 ± 0.2

Experimental data have been acquired using gas-oil and gas-water flows at pipe inclinations, θ, of 0° and 4° upward for various superficial velocities, defined for phase i as $U_{Si} = Q_i/A_P$ where Q is the volumetric flow rate and A_P the cross-sectional area of the annulus, $A_P = \pi(D_1^2 - D_2^2)/4$. Superficial gas velocities at inlet conditions, $U_{SG,inlet}$, were varied between 0.5 and 5 m/s and superficial liquid velocities, U_{SL}, between 0.2 and 2 m/s (see Table 3). Experiments were performed at steady-state conditions at a pressure of 400 kPa (absolute) and temperature of 21 ± 1 °C (for all flow conditions). It was found that the system pressure (400 kPa) used in this investigation has little effect on the viscosity of the liquids (*i.e.* water and Exxsol). Moreover, the temperature of the fluids was monitored and regulated using heat exchangers to avoid temperature effects on the fluid properties, such as viscous heating which, as contrary to our investigation, plays an important role in microflows (*e.g.* microchannels) as surface forces are dominant. The gas phase expands as it flows along the test section, especially for cases with high pressure drop. The local superficial gas velocity is calculated using the inlet to local gas density ratio, which in turn is function of the local pressure, as $U_{SG} = U_{SG,inlet}\,(\rho_{G,inlet}/\rho_{G,local})$. Results presented in this paper corresponds to local superficial gas velocities (U_{SG}) at the observation section ($L/D_h \approx 710$), unless explicitly stated otherwise.

Table 3: Experimental flow velocities for each flow configuration. Superficial gas velocities at inlet conditions are 0.5, 0.75, 1, 1.5, 2, 2.5, 3, 4 and 5 m/s.

U_{SL} (m/s)	$U_{SG,inlet}$ (m/s)	
	Concentric	Eccentric
0.2	0.5 - 2.5	0.5 - 4
0.4	0.5 - 4	0.5 - 4
0.6	0.5 - 4	0.5 - 4
0.8	0.5 - 4	0.5 - 5
1.0	0.5 - 4	0.5 - 5
1.2	0.5 - 3	0.5 - 5
1.4	0.5 - 3	0.5 - 4
1.6	0.5 - 3	0.5 - 4
1.8	0.5 - 3	0.5 - 4
2.0	0.5 - 3	0.5 - 2.5

2.4   Instrumentation

The test section was equipped with 5 differential pressure transducers (Fuji, Model FCX) installed along the pipe with an accuracy of ±6 Pa. Pressure transducers were located at $284D_h$, $410D_h$, $501D_h$, $649D_h$, and $719D_h$ from the inlet and measure the pressure drop, ΔP, over an axial length of $62D_h$, $40D_h$, $50D_h$, $38D_h$, and $64D_h$ respectively. The test section inlet pressure was measured with an absolute pressure sensor (Tecsis, Model P3276) with an accuracy of ±5 kPa. The instantaneous cross-sectional average holdup, H_L, was measured with 3 broad-beam gamma densitometers measuring the liquid holdup in the full pipe cross-section at a sampling frequency of 50 Hz for a total recording time of 100 s (simultaneously with the pressure transducers). These gamma densitometers were located at $L/D_h = 256$, 520, and 704 with L the distance from the inlet. Calibration of the gamma densitometers was performed by measuring the transmitted intensity for single-phase gas, oil and water. The respective intensity calibration (*e.g.* gas and oil) was then used to calculate the holdup for two-phase flows.

Four Photron Mini UX100 high-speed cameras were used to capture instantaneous images of the flow. Each camera has resolution of 1280×1024 pixels at a maximum frame-rate of 4 kHz. The cameras were mounted at $L/D_h = 124$, 540, 740, and 766. The first three cameras were

equipped with a 14-mm ultra-wide-angle lens and recorded at a frame-rate of 50 Hz to capture large-scale features. The fourth camera, equipped with a Nikkor 60-mm lens, was operated at a frame-rate of 1 kHz to capture fast, small-scale features.

2.5   Measurement Uncertainty

Uncertainty analysis of the measured quantities is based on the instruments' systematic errors and the standard deviation of the samples (to estimate the random standard uncertainty). The uncertainty of the calculated quantities is estimated from the uncertainty propagation of the measured values (Dieck, 2006), *e.g.* the uncertainty of the superficial liquid velocities is estimated from the uncertainty propagation of the pipe diameters and the volumetric flow rate. Table 4 shows the average uncertainty estimates of the measured and computed variables.

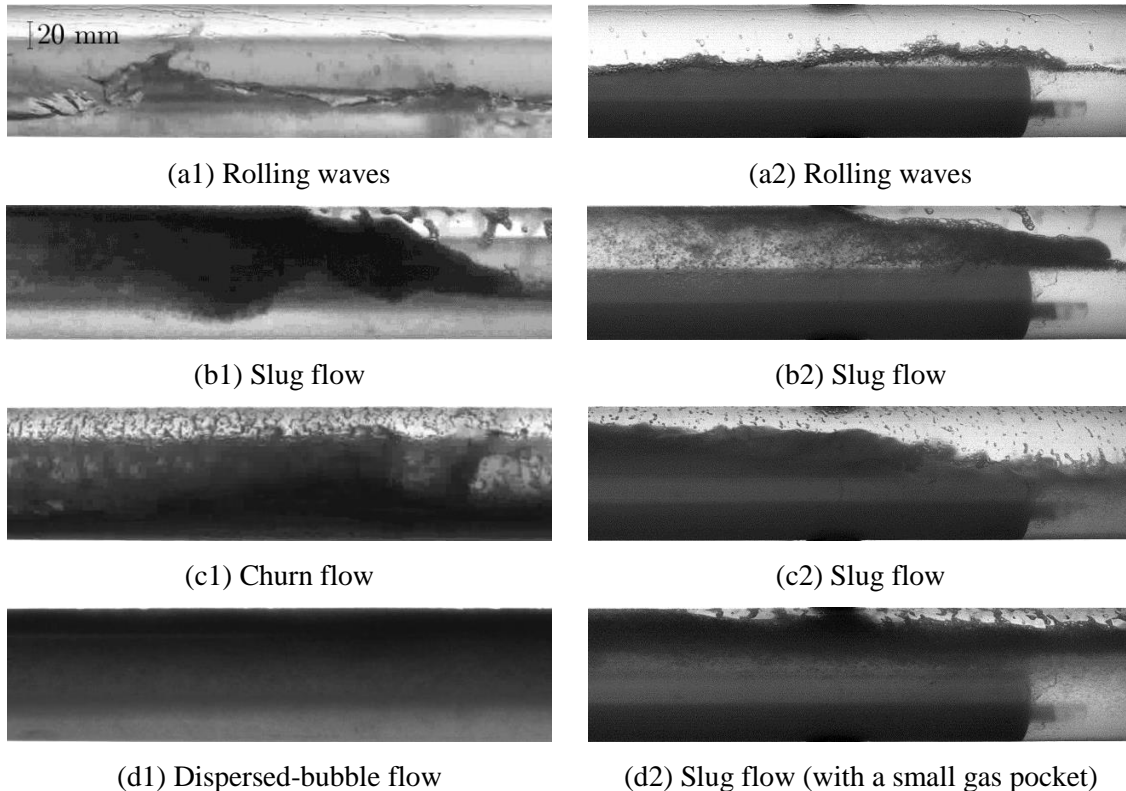**Table 4:** Measured and computed uncertainties for flow parameters.

	Variables	Uncertainty
Measured	D_1 (mm)	± 0.55 mm
	D_2 (mm)	± 0.28 mm
	θ (°)	$\pm 0.04°$
	ρ_G (kg/m^3)	± 0.5 kg/m^3
	ρ_L (kg/m^3)	± 1.5 kg/m^3
Computed	U_{SG} (m/s)	± 2.3 %
	U_{SL} (m/s)	± 1.7 %
	H_L	$\pm 1.5\%$
	$\Delta P/\Delta L$ (Pa/m)	$\pm 4.5\%$

3   Results and Discussion

3.1   Flow regime classification

The geometrical distribution or flow regimes of the phases is a key parameter in the analysis of two-phase flows. Even though flow regimes can be identified by visual observations; quantification of the observed features necessitates additional techniques, such as X-ray computed tomography (Harvel *et al.*, 1999), or gamma instruments.

Figure 4 shows examples of four main flow regimes that have been observed in this study depending on the range of gas and liquid flow rates in both concentric and eccentric annuli. The figure displays four main flow characteristics. Figure 4(a1 & a2) present the rolling wave regime, where the gas and liquid phases flow in separated layers with intermittent waves of high amplitude and velocity. Figure 4(b1 & b2) show the slug flow, where we observed gas pockets separated by slugs of liquid with dispersed small bubbles. In Figure 4(c1), the flow is similar to the slug flow without a clear phase separation or structure. This is called churn flow. Finally, in Figure 4(d1), we show the dispersed-bubble flow regime, where the gas phase is fully dispersed in the continuous liquid phase.

(a1) Rolling waves	(a2) Rolling waves
(b1) Slug flow	(b2) Slug flow
(c1) Churn flow	(c2) Slug flow
(d1) Dispersed-bubble flow	(d2) Slug flow (with a small gas pocket)

Figure 4: Flow regimes observed in the experimental campaign. Instantaneous flow images correspond to gas-water flow in a horizontal concentric annulus (left panel, denoted 1) and fully eccentric annulus (right panel, denoted 2) at: (a) $U_{SL} = 0.2$ m/s, $U_{SG,inlet} = 2.5$ m/s; (b) $U_{SL} = 1.0$ m/s, $U_{SG,inlet} = 0.75$ m/s; (c) $U_{SL} = 0.8$ m/s, $U_{SG,inlet} = 3.0$ m/s; and (d) $U_{SL} = 2.0$ m/s, $U_{SG,inlet} = 0.5$ m/s.

As shown in Figure 4, flow regimes in the eccentric annulus are often more consistent (*i.e.*

well-defined flow structures) than those observed in the concentric configuration, except for the dispersed-bubble flow regime. It seems that the amount of entrained gas in the liquid phase is lower in the eccentric annulus as compared to the concentric annulus for a given flow velocity. This suggests that the interface is more stable for the eccentric cases.

Past studies of annulus flows have mainly focused on vertical upward flow using air and water or low viscosity oils as the test fluids. The flow regime classification in vertical annulus flows is similar to that observed in circular pipes. Kelessidis and Dukler (1989) observed four basic flow regimes (bubble flow, slug flow, churn flow, and annular flow) in a vertical acrylic concentric and eccentric annulus (eccentricity 50%) test section with $D_1 = 76.2$ mm and $D_2 = 50.8$ mm using air and water as the test fluids. Flow regimes were classified using probability density function (PDF) analysis of the signals from conductivity probes. Caetano *et al.* (1992a) performed experiments in a concentric and fully eccentric annulus with $D_1 = 76.2$ mm (acrylic) and $D_2 = 42.2$ mm (PVC) using water and kerosene as the liquid phase and air as the gas phase. Flow regimes were classified using the same categories as Kelessidis and Dukler (1989) with the addition of dispersed flow (small spherical bubbles as compared with those observed in bubble flow).

In a horizontal setup, Wongwises and Pipathattakul (2006) identified 9 flow regimes for air-water flow in an acrylic concentric annulus with $D_1 = 12.5$ mm and $D_2 = 8$ mm. These flow regimes were: plug, slug, annular/slug, annular, bubble/plug, bubbly/slug-plug, churn, dispersed-bubble, and slug/bubble flow. Ozbayoglu and Yuksel (2012) performed experiments in an eccentric annulus with $D_1 = 74$ mm and $D_2 = 47$ mm. They observed stratified flows in addition to those regimes observed by Wongwises and Pipathattakul (2006) which were more influenced by capillary effects due to the small size of the annulus.

3.2   *Flow regime maps*

We have classified gas-liquid flow regimes using both visual observations from high-speed imaging (camera 3 located at $L/D_h = 740$) and probability density function (PDF) of the cross-

sectional holdup data recorded by a broad-beam gamma densitometer located at $L/D_h = 704$ (G3 on Figure 2). With this complementary approach it was possible to identify the flow regimes more objectively. Figure 5 shows time-series of the cross-sectional averaged holdup values and the corresponding PDF as function of the holdup normalised by the maximum value, $h = H/H_{max}$. Each of these figures presented in Figure 5 is listed according to visual observations displayed in Figure 4.

The PDF of rolling waves (RW) shows a single peak away from $h = 1$. Slug flows (SG) are characterised by two peaks in the PDF corresponding to the Taylor bubble region (peak at $h < 1$) and the liquid slug region (peak near $h = 1$). Churn flow (CH) shows a PDF distribution similar to that observed for rolling waves regime (*i.e.* single peak) but with a higher mean value of the normalised holdup, h. The variance of the single peak distribution is greater than that in rolling waves suggesting a more chaotic behaviour. Finally, dispersed-bubble (DB) flows show a narrow peak near $h = 1$. Even though the distribution in this case is close to a normal distribution, PDF of the cross-sectional averaged indicates a signal with high mean value with small variance as it can also be seen easily in Figure 5(d).
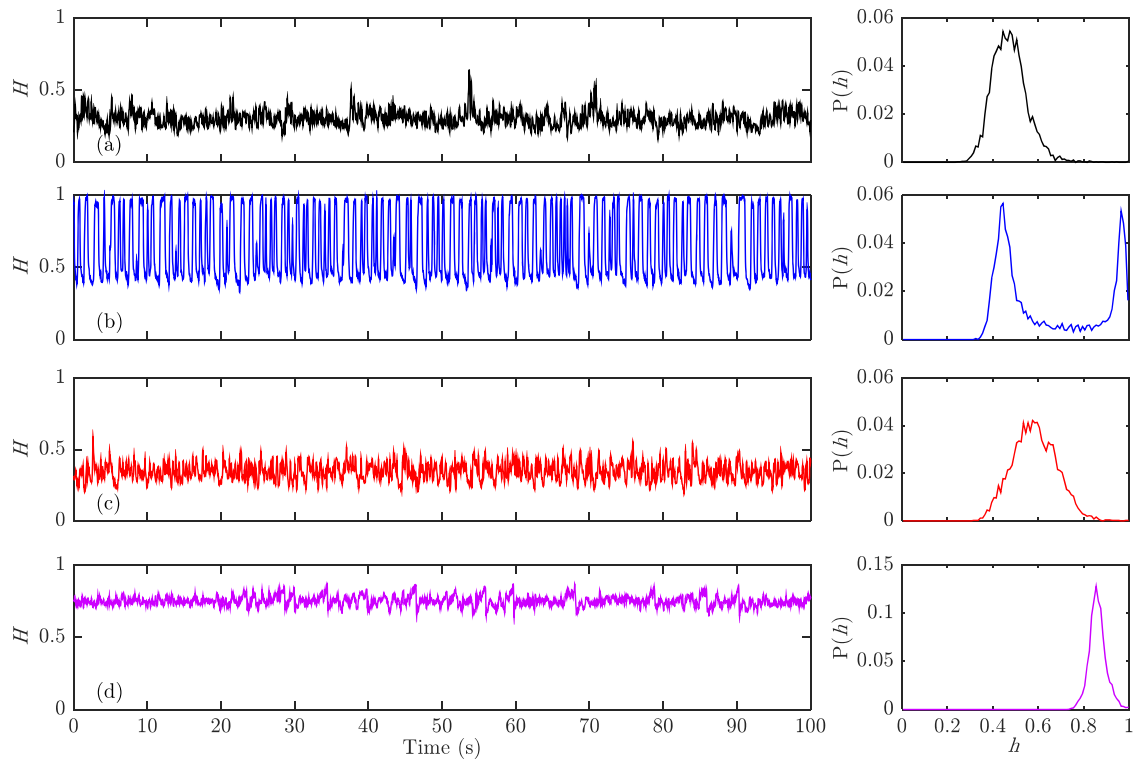
Figure 5: Typical evolution of the cross-sectional average holdup and PDF for the flow conditions shown in Figure 4 for gas-water flow in the concentric annulus: (a) rolling waves ($H_{max} = 0.64$), (b) slug flow ($H_{max} = 1.00$), (c) churn flow ($H_{max} = 0.59$), and (d) dispersed-bubble flow ($H_{max} = 0.87$).

In addition to the flow regimes presented in Figure 4, our close look at the available data from four cameras indicates the existence of transitional regions where the flow exhibits characteristics of more than one flow regime, for example, transition between slug and rolling waves (T-S/R) and the transition from intermittent to dispersed-bubble flow (T-DB). Analysis of the PDFs in these cases is found to be inconclusive due to absence of a well-defined flow regime. In these cases, our analysis is supplemented by the time traces of the cross-sectional averaged holdup values and the camera recordings. It is clear from the instantaneous signal that Figure 6(a) appears to be a superposition of typical signals for slug flow and rolling waves, which introduces a randomness component to the well-defined quasi-periodic time trace of slug flow. In a similar fashion, one can observe that Figure 6(b) displays a churn/slug and dispersed-bubble flow signal in combination.
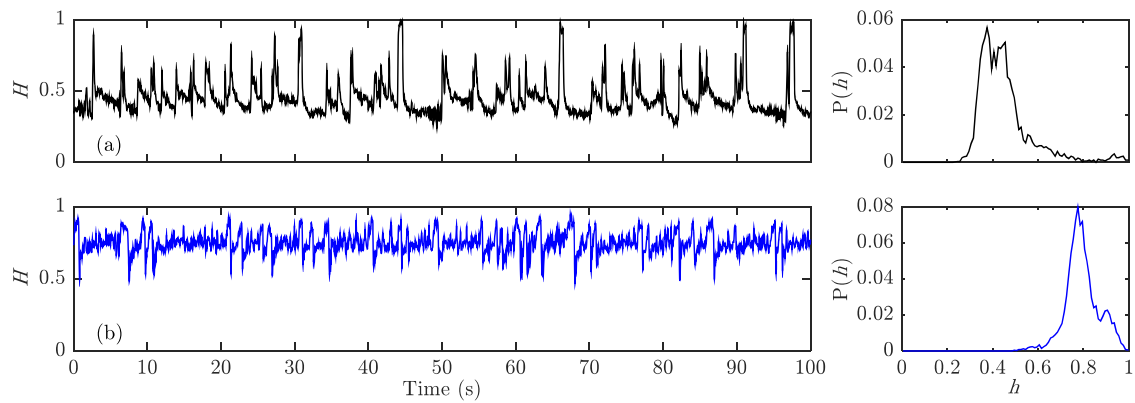
Figure 6: Typical evolution of the cross-sectional average holdup and PDF for: (a) transition slug/rolling waves (U_{SL} = 0.4 m/s, $U_{SG,inlet}$ = 1.5 m/s, H_{max} = 1.0), and (b) transition to dispersed-bubble (U_{SL} = 1.8 m/s, $U_{SG,inlet}$ = 0.5 m/s, H_{max} = 0.95). Flow conditions shown here correspond to gas-water flow in a horizontal concentric annulus.

We constructed flow regime maps (as can be seen in Figure 7 and Figure 8) for different conditions studied in this paper. For a horizontal annulus, rolling waves (separated flows) are observed at low liquid velocities and mid/high gas velocities. For a given gas velocity and increasing liquid velocity, the liquid content in these waves also increases leading to a transition to slug or churn flow.
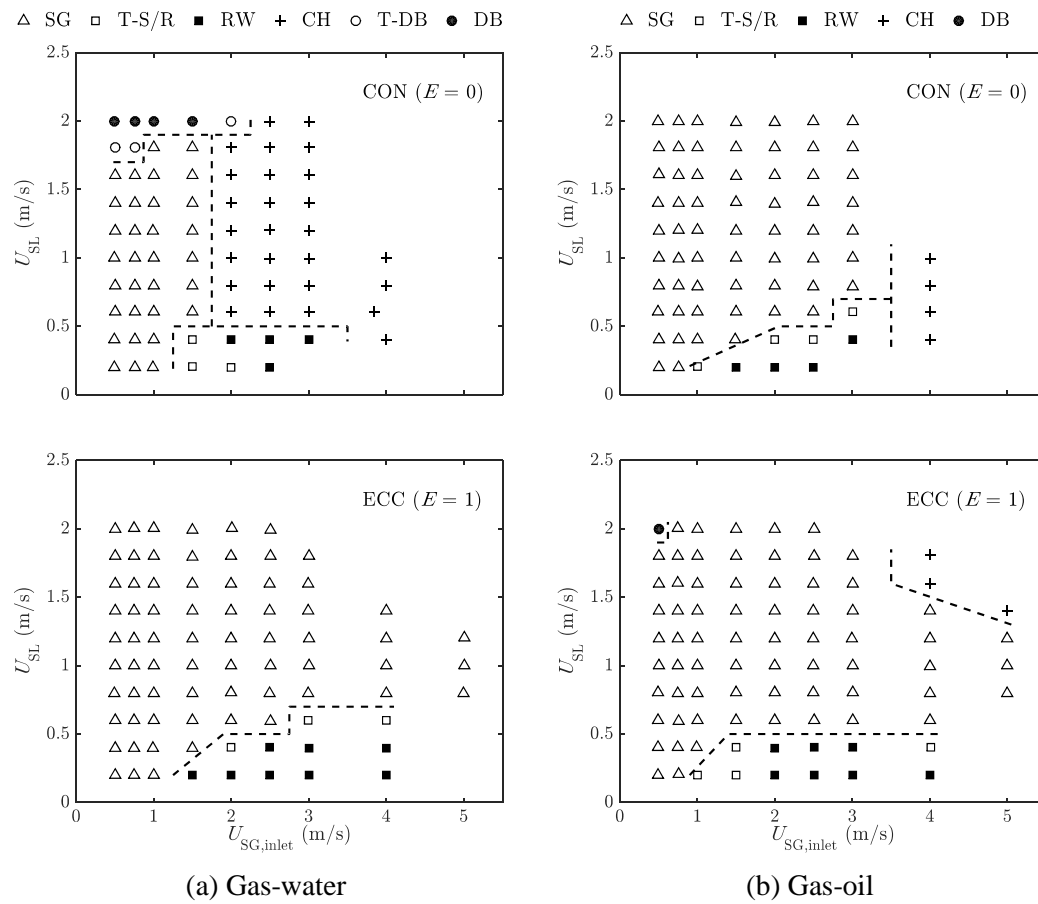
Figure 7: Flow regime maps at a horizontal pipe for concentric ($E = 0$) and fully eccentric ($E = 1$) annuli for: (a) gas-water (left column) and (b) gas-oil (right column).
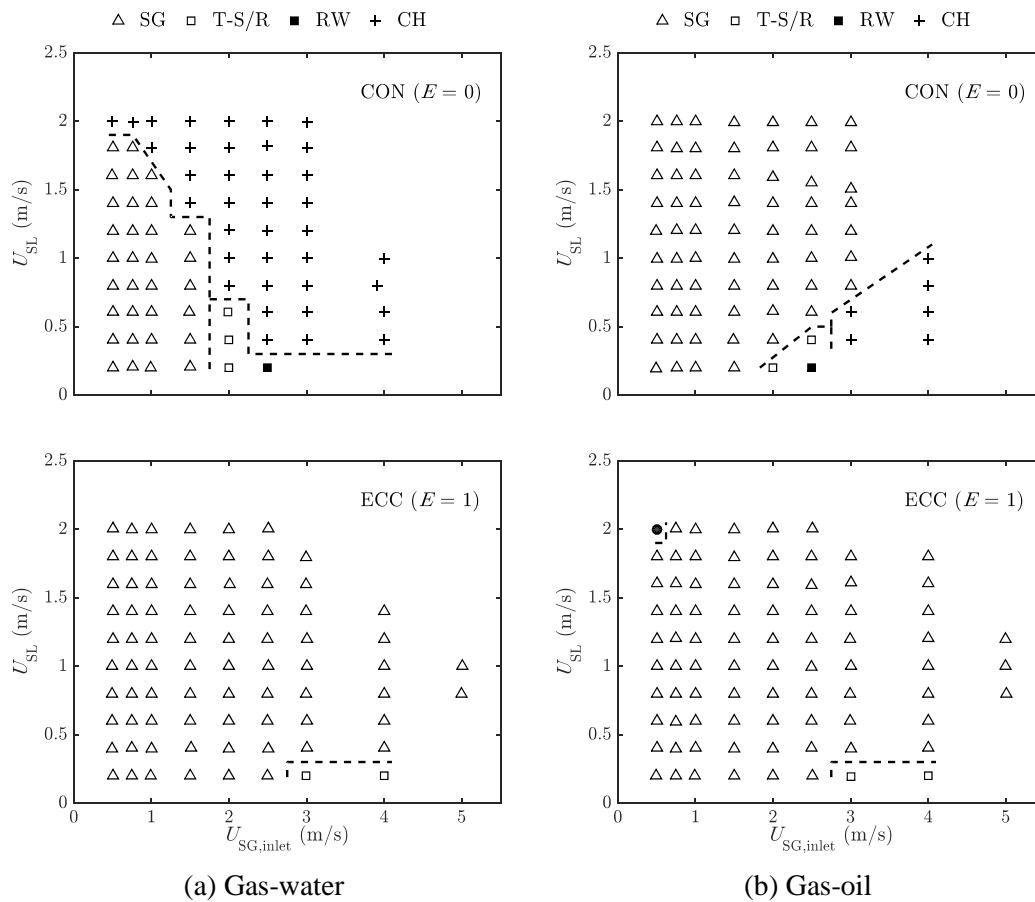
Figure 8: Flow regime maps at a pipe inclination of 4° for concentric ($E = 0$) and fully eccentric ($E = 1$) annuli for: (a) gas-water (left column) and (b) gas-oil (right column).

Slug flow dominates the flow map regardless of the flow configuration and geometry with exception of gas-water flows in the concentric annulus. For this configuration in both horizontal and inclined pipes, we observed churn flow over a wide range of flow velocities. This indicates that gas-oil flows have a more stable phase fraction behaviour across the cross-section than gas-water flows. For full pipe systems, as the surface tension decreases the droplet entrainment increases (Tayebi *et al.*, 2000; Mantilla *et al.*, 2012; Karami *et al.*, 2017). In our experiments the opposite behaviour is observed, and this can possibly be attributed to the wetting characteristics of the pipe (hydrophobic) which generate instabilities in the film region in slug flows with a larger effect in the concentric annulus configuration. The oil phase tends to fully wet the pipe as the gas velocity increases, creating a continuous film in the gas region. Conversely for gas-water flows, this thin film is not continuous, thus increasing the effective pipe roughness and promoting

unstable structures. In general, slug flows in the eccentric annulus are more stable than those observed in the concentric annulus, which we think can be attributed to the larger cross-sectional uninterrupted area (larger chord length).

The transition from slug to churn flows was also analysed using the structure (or bubble) velocity from cross-correlation of the time-evolution of the cross-sectional holdup from gamma sensors G2 and G3. For slug flow, the bubble velocity follows a linear trend and is well predicted using the Nicklin *et al.* (1962) expression where values of the distribution parameter and drift velocity depend on the fluids, pipe inclination and annulus eccentricity (see Ibarra and Nossen, 2018). It was found that, in general, the structure velocity for churn flow is lower than the linear trend found for well-defined slug flow conditions. This was also observed in full pipe systems (Lin and Hanratty, 1987; Parsi *et al.*, 2017; Soedarmo *et al.*, 2018).

At high liquid and low gas velocities, dispersed-bubble flow is observed only for gas-water concentric annulus (0°) and gas-oil eccentric annulus (0° and 4°). There is no apparent relation in occurrence of the dispersed-bubble flow for the flow combinations (gas-water and gas-oil) and annulus configurations studied (concentric and eccentric). At the transition between slug or churn and dispersed-bubble, the gas is dispersed in the continuous liquid flow with intermittent (non-periodic) gas pockets at the top of the pipe (as observed by the secondary peak at $h \approx 0.9$ in the PDF analysis in Figure 6(b)). These transition regions or bands are difficult to observe as the experimental test matrices have currently been constructed to cover wide velocity regions with large grid size.

For upward inclinations, occurrence of the rolling waves decreases as the transition to slug flow occurs at lower liquid velocities. This is attributed to the reduction in the liquid velocity, which in turn increases the liquid holdup. Moreover, for a given liquid velocity the transition from slug flow to rolling waves occurs at higher gas velocities for upward inclinations, as a higher gas velocity is required to overcome the effect of gravity on the liquid film (back flow). At the transition between slug flow and rolling waves the flow exhibits characteristics of two different regimes as shown in the PDF analysis above (see Figure 6(a)). The flow shows rolling

waves with intermittent liquid slugs with no defined frequency and length. For gas-water flow in concentric annulus (at $\theta = 4°$), the U_{SG} at the transition between slug and churn flow decreases as U_{SL} increases. It is hypothesised that as more liquid is introduced in the system for a given gas velocity, gravitational forces, in addition to the wetting effects (in concentric annulus), are enough to break the film and generate unstable flows.

3.3   Liquid holdup

Figure 9 shows the mean liquid holdup, H_L, (read by gamma sensor 3 in Figure 2) as function of the no-slip liquid fraction, Φ_L, for gas-water and gas-oil flows both in concentric and fully eccentric annuli when the pipe is horizontal. Presented data consist of four different superficial liquid velocities. The no-slip liquid fraction is defined as $\Phi_L = U_{SL}/U_M$ with the mixture velocity $U_M = U_{SG} + U_{SL}$. In this calculation, the superficial gas velocity is corrected for expansion based on the pressure drop along the test section. Eccentric annulus flow shows slightly higher holdup values than those observed in the concentric annulus configuration. This liquid accumulation in the eccentric annulus can certainly be attributed to a low speed created by the narrow gap between the outer and the inner pipe at the bottom of the outer pipe (see Jonsson and Sparrow, 1966; and Choueiri and Tavoularis, 2014; for single-phase flow in similar geometries).

Measured data indicate that there are no significant differences in liquid holdup between two-phase flow with SF6/Exxsol D60 and SF6/water. The only exception is at lower U_{SL} (*i.e.* $U_{SL} = 0.2$ m/s). This difference might be attributed to the occurrence of different flow regimes for otherwise similar flow conditions in both flow configurations. The existence of different flow regimes depends on several variables, namely flow conditions, geometrical parameters, and the physical properties of the fluids (*e.g.* density, viscosity, and surface tension). The lower surface tension for gas-oil flows enhances the gas bubble formation and could be a reason for the difference in liquid holdup. However, from our experiments, the observed trends cannot be fully attributed to surface tension alone, as there are other varying parameters such as annulus

eccentricity. Moreover, the wetting characteristics also seem to have an influence in the behaviour of the flow as described in Section 3.2.
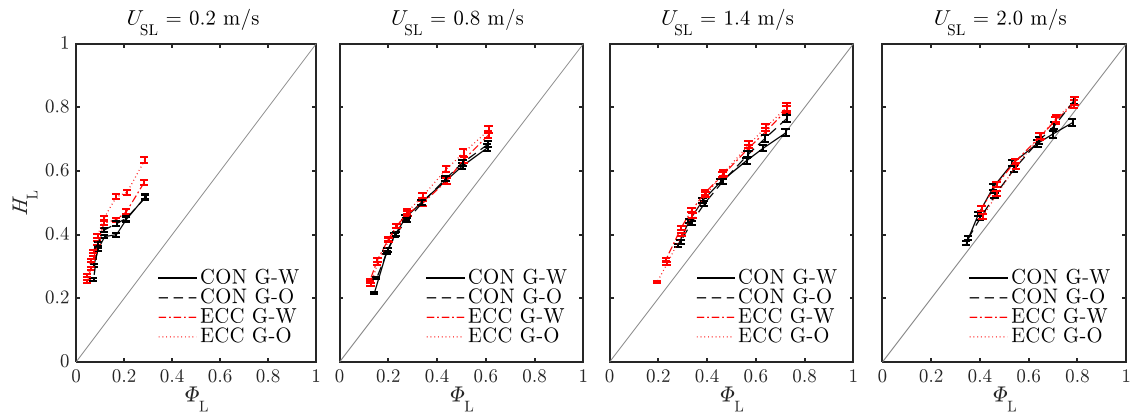
Figure 9: Mean liquid holdup, H_L, as function of the no-slip liquid fraction, Φ_L, at horizontal concentric and fully eccentric annuli for gas-water and gas-oil flows at different superficial liquid velocities, U_{SL}.

Figure 10 shows a comparison of the mean holdup for different pipe inclinations (0° and 4°). These figures reveal that the holdup is independent of the pipe inclination, even for the lowest U_{SL}, for the range of pipe inclinations studied here. When gravitational forces dominate over inertial forces, the liquid velocity decreases, increasing the liquid holdup closer to the inlet with back flow further downstream (low holdup). This back flow or recirculation (observed at $U_{SL} = 0.2$ m/s) leads to a flow regime transition from separated flow (*e.g.* rolling waves) at 0° to slug flow at 4°. However, the time-averaged holdup for both pipe inclinations is similar.
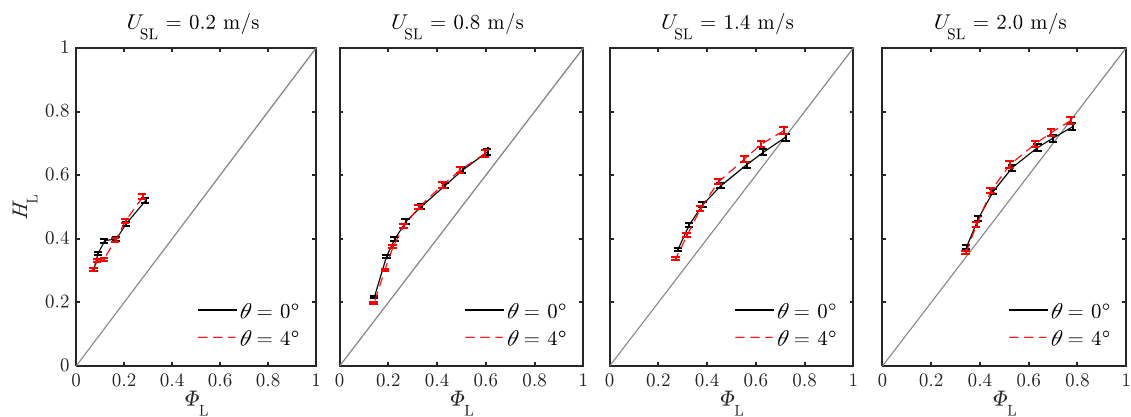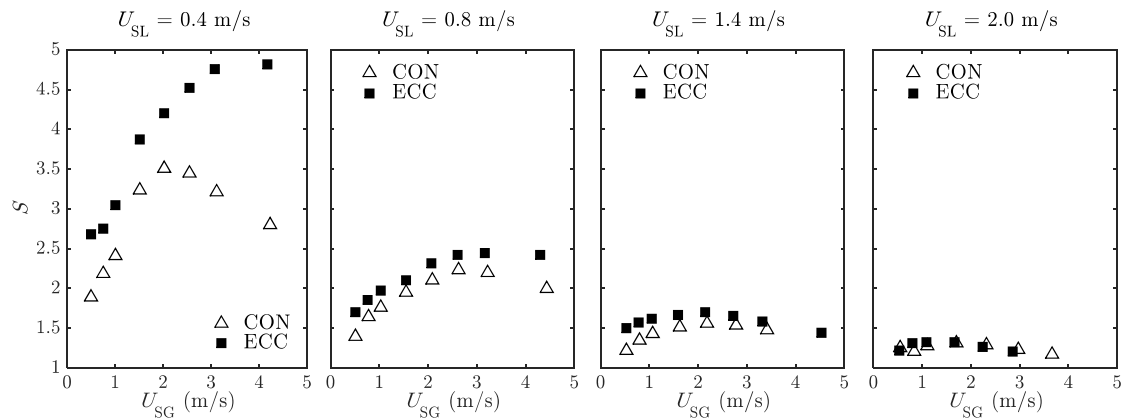

Figure 10: Mean liquid holdup, H_L, as function of the no-slip liquid fraction, Φ_L, for gas-water in a concentric annulus at pipe inclinations, θ, of 0° and 4°.

Analysis of the local average velocities offers further insight into the slippage or velocity difference between both phases. In gas-liquid flows, the gas phase usually flows faster than the liquid because of buoyancy (especially for vertical flows) and lower frictional losses. This means that the local liquid holdup is higher than the no-slip liquid fraction (as observed in Figure 9 and Figure 10). However, for dispersed flows with high liquid and low gas flow rates the gas phase can travel at approximately the same velocity as the liquid, thus the slip ratio, *S*, is very nearly equal to unity. Our calculation of the slip ratio takes into account the expansion of the gas due to pressure losses from the inlet section to the location of each gamma sensor. The slip ratio is defined as the ratio of the local average gas to liquid velocity and can be computed from

$$S = \frac{u_G}{u_L} = \left(\frac{1 - \Phi_L}{\Phi_L}\right)\left(\frac{H_L}{1 - H_L}\right). \tag{1}$$

Figure 11 shows a comparison of the slip ratio as a function of the superficial gas velocity between concentric and fully eccentric annuli for horizontal gas-oil flows. In general, the gas flows faster than the liquid ($S > 1$) with the largest difference at low U_{SL}. The slip ratio decreases as the superficial liquid velocity increases. For $U_{SL} \leq 1.4$ m/s, the slip ratio for eccentric annulus flows is higher than that observed for the concentric annulus configuration at the same flow velocity. This is attributed, as mentioned above, to the low velocity region at the bottom of the pipe (narrow gap region) in the eccentric annulus configuration. This behaviour is more prominent at low liquid flow rates, as phases flow in separated layers (with small or no gas entrainment in the liquid layer).
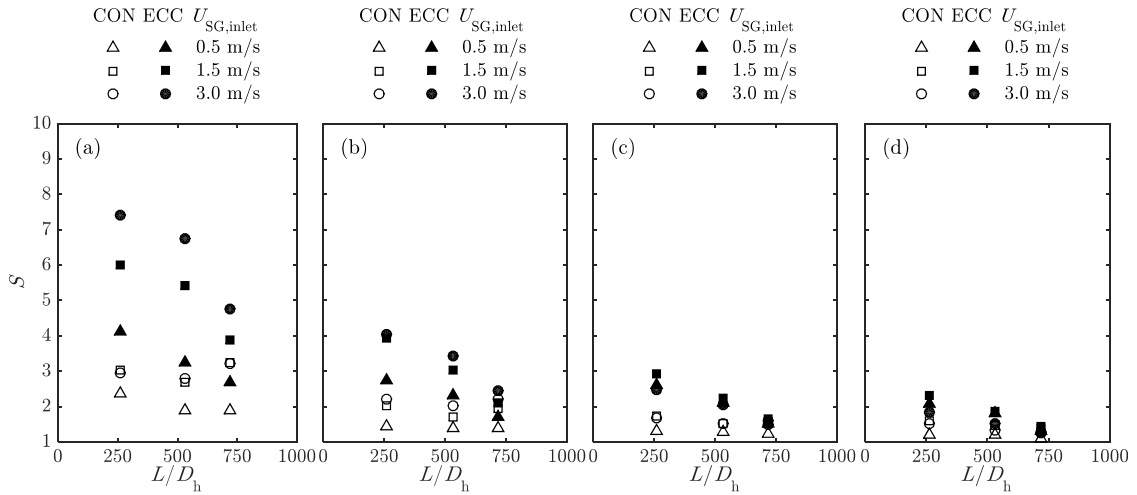
Figure 11: Slip ratio, *S*, as function of superficial gas velocity, U_{SG}, at horizontal concentric and fully eccentric annuli for gas-oil flows at different superficial liquid velocities, U_{SL}.

3.3.1   Evolution of the liquid holdup

Broad-beam gamma densitometers installed along the test section allow the investigation of the evolution of the liquid holdup with respect to the distance from the inlet (L/D_h). Figure 12 shows the slip ratio at the location of each gamma densitometer at different flow conditions for gas-oil concentric and fully eccentric horizontal annuli. Two different trends can be observed: (i) for the concentric annulus, the slip ratio seems to be fairly independent of L/D_h with exception of Figure 12(a), which corresponds to low frequency slugs and rolling-wave regime; and (ii) for the fully eccentric annulus, the slip ratio decreases with increasing L/D_h.

The evolution of the slip ratio (or liquid holdup) along the test pipe offers an insight into the development of the flow for concentric and eccentric annuli. This suggests that the flow reaches developed conditions faster in the concentric annulus configuration than in the fully eccentric configuration. The inlet effects persist longer in eccentric annuli due to the low speed region created at the bottom wall of the outer pipe. The flow in low speed regions may be more stable because viscous effects dominate the flow and prevent disturbances from growing, although this remains to be proven. This eventually leads to less turbulence and less mixing. In the end, we observe that the initial and boundary conditions set at the inlet show their footprint at locations further downstream.

Figure 12: Slip ratio, *S*, as function of L/D_h for horizontal gas-oil flow at concentric and fully eccentric annuli at: (a) $U_{SL} = 0.4$ m/s, (b) $U_{SL} = 0.8$ m/s, (c) $U_{SL} = 1.4$ m/s, and (d) $U_{SL} = 2.0$ m/s.

3.4   Pressure gradient

Figure 13 shows the frictional pressure gradient data for gas-water concentric and fully eccentric annuli at an inclination of 0° and 4° as function of the mixture velocity, U_M. The frictional pressure gradient (for inclined flows) is calculated from

$$\left[\frac{\Delta P}{\Delta L}\right]_{Fric} = \left[\frac{\Delta P}{\Delta L}\right]_{Total} - \rho_M g \sin\theta \tag{2}$$

where *g* is the gravitational acceleration and ρ_M is the mixture density,

$$\rho_M = \rho_L H_L + \rho_G (1 - H_L). \tag{3}$$

In general, the pressure loss in the concentric annulus is higher than in the fully eccentric annulus for all flow conditions studied. Moreover, for a given U_{SL}, the difference in the pressure gradient between concentric and fully eccentric annuli appears to increase with increasing mixture velocity (*i.e.* increasing the gas flow rate). This behaviour was also observed for gas-oil flows and can be attributed to the distribution of the liquid around the pipe in the film region for slug/churn flows, *i.e.* the liquid starts to arrange in an annular configuration for concentric annulus at lower gas velocities than in fully eccentric annulus for a given liquid flow rate.

The frictional pressure loss for $\theta = 4°$ is similar, and for some cases slightly higher (especially for concentric anulus), than for horizontal flow. However, for low U_{SL} and a given

eccentricity (see Figure 13(a)), frictional losses significantly increase with the pipe inclination for cases where back flow was observed.
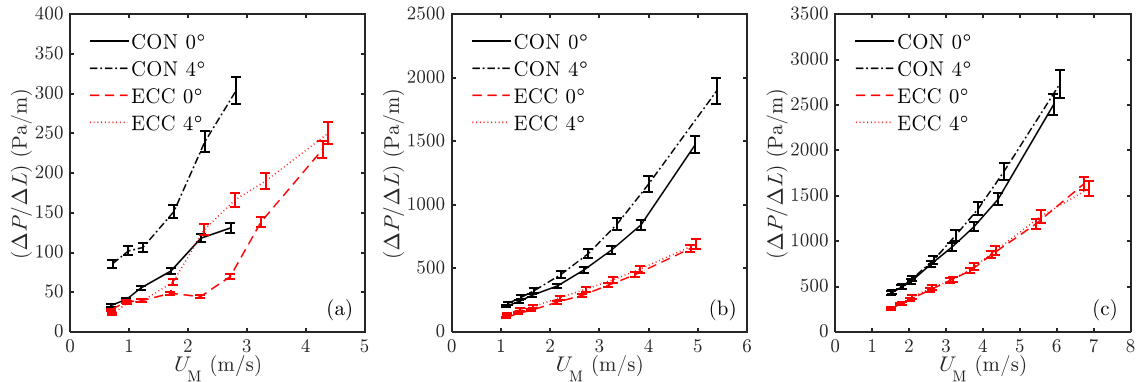
Figure 13: Frictional pressure gradient, $\Delta P/\Delta L$, as function of the mixture velocity, U_M, for gas-water flow in concentric and fully eccentric annuli at 0° and 4° pipe inclination and superficial liquid velocities of: (a) $U_{SL} = 0.2$ m/s, (b) $U_{SL} = 0.6$ m/s, and (c) $U_{SL} = 1.0$ m/s.

4   Conclusions

Experimental investigations have been performed in concentric and fully eccentric annuli studying gas-water and gas-oil flows at horizontal and 4° upward pipe inclination. The experiments focused on annulus flow with large outer pipe diameters, a dense gas phase, and high-pressure systems to better simulate the conditions corresponding, for example, to horizontal wells with inflow control. The flow has been studied using high-speed photography, differential pressure sensors, and gamma densitometers installed at different positions (L/D_h) from the inlet.

Flow regimes have been identified using visual observations from the high-speed cameras and probability density function of the evolution of the cross-sectional average holdup from the gamma densitometer. These probability distributions show particular features for each flow regime, *e.g.* slug flows are characterised by two peaks in the probability distribution profile. Four main flow regimes have been identified over the range of gas and liquid velocities studied: rolling waves, slug flow, churn flow, and dispersed-bubble flow. The structure of the flow in the eccentric annulus is more stable than that observed in the concentric configuration. This might be attributed to a difference in the velocity distribution due to the position of the inner pipe, *i.e.* a

wider gap for fully eccentric annulus. Furthermore, gas-water flows in the concentric annulus show chaotic or unstable behaviour in regions dominated by slug flow compared to other annulus configurations and flow combinations. One reason for this behaviour might be attributed to the wetting characteristics of the pipe, *i.e.* the oil tends to wet the pipe creating a continuous thin film at the pipe wall in the gas region for high gas velocities, whereas for water flows, this film is not continuous.

Data on the liquid holdup from the downstream gamma densitometer show no significant differences between gas-water, gas-oil, concentric, and fully eccentric annulus. However, data on the slip ratio show higher values at low U_{SL} for the eccentric cases as compared to those in the concentric annulus. Moreover, flow development along the test section is observed in some cases. For the concentric annulus, the local liquid holdup (and the slip ratio) is nearly constant with L/D_h. In contrast, H_L (or the slip ratio) gradually decreases along the test section for fully eccentric annulus.

The pressure gradient in the concentric annulus is higher than in fully eccentric annulus for the same flow conditions. The acquired experimental data aim to improve our fundamental understanding of multiphase flow in annulus pipes, as no experimental or theoretical models are available in the literature for the type of flows studied in this work.

References

Caetano, E.F., Shoham, O., Brill, J.P. (1992a) Upward vertical two-phase flow through an annulus-Part I: Single-phase friction factor, Taylor buble rise velocity, and flow pattern prediction. J. Energy Resour. Technol., 114(1), 1-13.

Caetano, E.F., Shoham, O., Brill, J.P. (1992b) Upward vertical two-phase flow through an annulus-Part II: Modeling bubble, slug, and annular flow. J. Energy Resour. Technol., 114(1), 1-17.

Choueiri, G.H., Tavoularis, S. (2014) Experimental investigation of flow development and gap vortex street in an eccentric annular channel. Part 1. Overview of the flow structure. J. Fluid Mech., 752, 521-542.

Das, G., Das, P.K., Purohit, N.K., Mitras, A.K. (1999) Flow pattern transition during gas liquid upflow through vertical concentric annuli-Part I: experimental investigations. J. Fluids Eng., 121, 895-901.

Dieck, R.H., 2006. Measurement Uncertainty: Methods and Aplications, Fourth ed. ISA.

Dou, H., Khoo, B., Tsai, H. (2010) Determining the critical condition for turbulent transition in a fully developed annulus flow. J. Pet. Sci. and Eng., 73, 41-47.

Ekberg, N.P., Ghiaasiaan, S.M., Abdel-Khalik, S.I., Yoda, M., Jeter, S.M. (1999) Gas–liquid two-phase flow in narrow horizontal annuli. Nucl. Eng. Des., 192, 59-80.

Hanks, R.W., Bonner, W.F. (1971) Transitional Flow Phenomena in Concentric Annuli. Ind. Eng. Chem. Fundam., 10, 105.

Harvel, G.D., Hori, K., Kawanishi, K., Chang, J.S. (1999) Cross-sectional void fraction distribution measurments in a vertical annulus two-phase flow by high speed X-ray computed tomography and real-time neutron radiography techniques. Flow Meas. Instrum., 10, 259-266.

Hasan, A.R., Kabir, C.S. (1992) Two-phase flow in vertical and inclined annuli. Int. J. Multiph. Flow, 18(2), 279-293.

Hibiki, T., Situ, R., Mi, Y., Ishii, M. (2003) Local flow measurements of vertical upward bubbly flow in an annulus. Int. J. Heat Mass Tran., 46(1479-1496).

Hu, B., Langsholt, M., Nuland, S., Lawrence, C.J. (2009) Void distribution in the liquid layer in stratified wavy flows measured with an X-ray Computed Tomography instrument. 14th Int. Conf. on Multiphase Prod. Tech., Cannes, France.

Hu, B., Nuland, S., Nossen, J., Langsholt, M., Lawrence, C.J. (2010) Entrainment of gas into slugs and its subsequent transport in two-phase slug flow. 7th North American Conf. on Multiphase Tech., Banff, Canada.

Ibarra, R., Nossen, J. (2018) Bubble velocity in horizontal and low-inclination upward slug flow in concentric and fully eccentric annuli. Chem. Eng. Sci., 192, 774-787.

Jonsson, V.K., Sparrow, E.M. (1966) Experiments on turbulent-flow phenomena in eccentric annular ducts. J. Fluid Mech., 25, 65-86.

Julia, J.E., Ozar, B., Jeong, J.-J., Hibiki, T., Ishii, M. (2011) Flow regime development analysis in adiabatic upward two-phase flow in a vertical annulus. Int. J. Heat Fluid Flow, 32, 164-175.

Karami, H., Pereyra, E., Torres, C.F., Sarica, C. (2017) Droplet entrainment analysis of three-phase low liquid loading flow. Int. J. Multiph. Flow, 86, 45-56.

Kelessidis, V.C., Dukler, A.E. (1989) Modeling flow pattern transitions for upward gas-liquid flow in vertical concentric and eccentric annuli. Int. J. Multiph. Flow, 15(2), 173-191.

Kelessidis, V.C., Dukler, A.E. (1990) Motion of large gas bubbles through liquids in vertical concentric and eccentric annuli. Int. J. Multiph. Flow, 16, 375-390.

Lin, P.Y., Hanratty, T.J. (1987) Detection of slug flow from pressure measurements. Int. J. Multiph. Flow, 13, 13-21.

Mantilla, I., Kouba, G., Viana, F., Roberts, R. (2012) Experimental investigation of liquid entrainment in gas at high pressure. 8th North American Conference on Multiphase Technology, Banff, Alberta, Canada.

Nicklin, D.J., Wilkes, J.O., Davidson, J.F. (1962) Two-phase flow in vertical tubes. Trans. Inst. Chem. Eng., 40, 61-68.

Osamasali, S.I., Chang, J.S. (1988) Two-phase flow regime transition in a horizontal pipe and annulus flow under gas–liquid two-phase flow. ASME FED, 72, 63-69.

Ozar, B., Jeong, J.-J., Dixit, A., Julia, J.E., Hibiki, T., Ishii, M. (2008) Flow structure of gas-liquid two-phase flow in an annulus. Chem. Eng. Sci., 63, 3998-4011.

Ozbayoglu, A., Yuksel, H.E. (2012) Analysis of gas-liquid behaviour in eccentric horizontal annuli with image processing and artificial intelligence techniques. J. Pet. Sci. and Eng., 81, 31-40.

Parsi, M., Azzopardi, B.J., Al-Sarkhi, A., Kesana, N.R., Vieira, R.E., Torres, C.F., McLaury, B.S., Shirazi, S.A., Schleicher, E., Hampel, U. (2017) Do huge waves exist in horizontal gas-liquid pipe flow? Int. J. Multiph. Flow, 96, 1-23.

Soedarmo, A., Soto-Cortes, G., Pereyra, E., Karami, H., Sarica, C. (2018) Analogous behavior of pseudo-slug and churn flows in high viscosity liquid system and upward inclined pipes. Int. J. Multiph. Flow, 103, 61-77.

Sveen, J.K. (2013) Laser Doppler anemometry (LDA) and particle image velocimetry (PIV) for marine environments. In Subsea Optics and Imaging, eds. Watson, J. and Zielinski, O., 14, 353-373.

Tayebi, D., Nuland, S., Fuchs, P. (2000) Droplet transport in oil/gas and water/gas flow at high gas densities. Int. J. Multiph. Flow, 26, 741-761.

Wongwises, S., Pipathattakul, M. (2006) Flow pattern, pressure drop and void fraction of two-phase gas-liquid flow in an inclined narrow annular channel. Exp. Thermal and Fluid Sci., 30, 345-354.